SCIENTIFIC REPORTS

OPEN

Magnetotransport and conductivity mechanisms in $Cu_2ZnSn_xGe_{1-x}S_4$ single crystals

Received: 8 May 2018
Accepted: 1 November 2018
Published online: 30 November 2018

Erkki Lähderanta[1], Elena Hajdeu-Chicarosh[1,2], Maxim Guc[1,2], Mikhail A. Shakhov[1,3], Ivan Zakharchuk[1], Ivan V. Bodnar[4], Ernest Arushanov[2] & Konstantin G. Lisunov[1,2]

Resistivity, ρ(*T*), and magnetoresistance (MR) are investigated in the $Cu_2ZnSn_xGe_{1-x}S_4$ single crystals, obtained by the chemical vapor transport method, between $x = 0$–0.70, in the temperature range of $T \sim 50$–300 K in pulsed magnetic field of B up to 20T. The Mott variable-range hopping (VRH) conductivity is observed within broad temperature intervals, lying inside that of $T \sim 80$–180 K for different x. The nearest-neighbor hopping conductivity and the charge transfer, connected to activation of holes into the delocalized states of the acceptor band, are identified above and below the Mott VRH conduction domain, respectively. The microscopic electronic parameters, including width of the acceptor band, the localization radius and the density of the localized states at the Fermi level, as well as the acceptor concentration and the critical concentration of the metal-insulator transition, are obtained with the analysis of the ρ(*T*) and MR data. All the parameters above exhibit extremums near $x = 0.13$, which are attributable mainly to the transition from the stannite crystal structure at $x = 0$ to the kesterite-like structure near $x = 0.13$. The detailed analysis of the activation energy in the low-temperature interval permitted estimations of contributions from different crystal phases of the border compounds into the alloy structure at different compositions.

In the last years, utilization of the Cu-based group I_2-II-IV-VI_4 chalcogenide semiconductors became one of the leading streams in the development of the low-cost thin film solar cells. Different stages have been overcame, and the recent one is based on a partial substitution of different cations in the standard Cu_2ZnSnS_4 (CZTS) compound[1–4]. This approach was found to lead to a substantial decrease of the detrimental defects in CZTS, increasing the device efficiency[1–4]. One of the most discussed elements to be add in CZTS is germanium, replacing partially tin. In this framework, several papers demonstrating a positive Ge effect on the solar cell efficiency have appeared recently[4–8]. In addition, the $Cu_2ZnSn_xGe_{1-x}S_4$ (CZTGS) solid solutions exhibit an increase of the band gap, E_g, with increasing Ge concentration, reaching the values of E_g up to ~2.3 eV for the pure Cu_2ZnGeS_4 (CZGS) compound[9,10]. This allows fine band gap tuning in the CZTGS solid solutions[6,11–13]. Such effect was found to be interesting for the multi-junction solar cells, where CZTGS could be used as a top solar cell[14].

In addition to photovoltaics, the structural and optical properties of CZTGS[11,13,15–17], as well as the vibrational properties of this material[16–19] have been studied. On the other hand, investigations of the electronic transport in CZTGS solid solutions are lacking up to date. The only available data have been obtained in the pure CZTS[20–23] and CZGS[24,25] border compounds. The latter was found to be crystalized in the kesterite (KS)[26] and wurtzstannite (WS)[27] types of structure, and the electronic properties were studied for each type of CZGS[24,25]. Both CZTS and CZGS compounds exhibit similar activated character of the temperature dependence of resistivity, including the Mott variable range hopping (VRH) conduction within a wide temperature range[22–25]. However, the behavior of magnetoresistance (MR) in these compounds is different, being completely positive (pMR) in CZTS[22] and possessing a negative contribution (nMR) in CZGS[24]. Therefore, similar activated conductivity with the Mott VRH conduction within a broad temperature range is expectable for the CZTGS solid solutions, too.

In the present work, investigations of the resistivity, ρ(*T*), and MR have been performed in $Cu_2ZnSn_xGe_{1-x}S_4$ with different x or Sn/(Sn + Ge) ratio values. The purpose is to establish the conductivity mechanisms in various

[1]Department of Physics, Lappeenranta University of Technology, PO Box 20, FIN-53851, Lappeenranta, Finland. [2]Institute of Applied Physics, Academiei Str. 5, MD-2028, Chisinau, Republic of Moldova. [3]Ioffe Institute, Politehnicheskaya Str. 26, St. Petersburg, 194021, Russian Federation. [4]Department of Chemistry, Belarusian State University of Informatics and Radioelectronics, P. Brovki Str. 6, Minsk, 220013, Belarus. Correspondence and requests for materials should be addressed to K.G.L. (email: kgl-oficial@hotmail.com)

x	Cu (at. %)	Zn (at. %)	Sn (at. %)	Ge (at. %)	S (at. %)	Cu/(Zn + Sn + Ge)	Zn/(Sn + Ge)	Cu/Zn
0.00	25.04	12.10	0.00	11.87	50.99	1.04	1.02	2.07
0.13	25.38	12.01	1.50	10.03	51.08	1.08	1.04	2.11
0.51	27.05	12.96	6.44	6.21	47.34	1.06	1.02	2.09
0.70	23.94	12.39	8.64	3.75	51.28	0.97	1.00	1.93

Table 1. Chemical composition of the investigated $Cu_2ZnSn_xGe_{1-x}S_4$ samples.

temperature intervals. Second goal of our work is to determine important microscopic electronic parameters of the material, depending on x. Such dependences are expected to be sensitive to crystal structure details and may yield valuable information on the phase content of the investigated material.

Materials and Methods

Single crystals of the $Cu_2ZnSn_xGe_{1-x}S_4$ solid solutions with $x = 0$–0.70 were grown by a chemical vapor transport method, with preliminary synthesis of the constituent elements in the vertical two zone furnace. The synthesized ingot was grinded and placed in the evacuated ampoule together with 5 mg/cm^3 of iodine, which was used as a transporter. The evaporation temperature was about 80 K below the growing temperature (~ 970 K). More details about the growing process can be found elsewhere[11,13,18]. As a result, four samples with different Ge/Sn ratio ($x = 0$, 0.13, 0.51 and 0.70) were selected for the subsequent analysis.

The structural and Raman scattering analyses of the samples taken from the same set have been performed previously, and the results can be found in ref.[18]. The structural analysis showed that all samples were crystalized in the tetragonal lattice, permitting exclusion of the WS phase. However, the results of ref.[18] did not yield a certain structural type of our samples, namely the KS or stannite (SN) one, which is a well-known problem of the Cu-Zn based quaternaries[28–30]. On one hand, the Raman scattering data could help to solve this problem, since an additional A-symmetry peak appears in the KS type materials compared to SN[26]. On the other hand, such additional Raman peak was significantly smaller comparing to other peaks in all analyzed samples[18,26]. From these results, it is not possible to exclude the existence of either KS or SN type structure in our samples. Additionally, as expected for single crystals, a good crystalline quality and absence of any secondary phases were found[18].

Chemical composition of selected samples was obtained using the energy dispersive X-ray microanalysis (EDAX). The composition of all samples was measured at least in five points, and the mean values are collected in Table 1. Here, we found that the real Sn/(Sn + Ge) ratio is quite close to the initial. In turn, the ratio of all cations is also quite close to the stoichiometric values (see three last columns in Table 1).

The hot probe method, addressed to thermopower measurements, demonstrated the p-type conductivity in all the investigated CZTGS samples. The resistivity and MR were measured with a standard dc method using six indium contacts. A pulsed magnetic field (PMF) was applied for the MR measurements, and the sample temperature was controlled using a nitrogen-filled cryostat. A dual compensation method, including the hardware and the software component, was used in order to avoid any induced voltage pertinent of the PMF measurements. More details about the PMF measurement procedure and the installation parameters could be found elsewhere[22].

Results and Discussion

Experimental results. As can be seen in Fig. 1, the dependence of $\rho(T)$ is activated in all samples, weakening between $x = 0$ and 0.13 and strengthening with increasing x between 0.13–0.70. Such behavior is attributable to a different proximity of samples to the metal-insulator transition (MIT) at different x, which will be verified later. In addition, the dependence of ρ on x is also different within two intervals of the composition. This is visible in the inset to Fig. 1, where $\rho(x)$ exhibits a sharp increase between $x = 0$–0.13 and weakening with further increasing x at any T, especially at high temperatures. Preliminarily, such behavior is attributable to a possible existence of the SN phase at $x = 0$, which is expectable in the pure CZGS compound, as well as the KS phase (see Section "Materials and Methods"). However, the SN phase is usually less stable than the KS phase[29,31]. So, in CZTGS it becomes unstable even at a small Sn content, transforming probably into a KS-like phase already at $x = 0.13$. Therefore, further evolution of the material properties should be smoother, reflecting only differences between the KS phases of the border compounds. This agrees with weakening of the $\rho(x)$ dependence above $x = 0.13$. Such conjecture, addressed to a deeper discussion of the resistivity depending on T and x, will be verified below, too.

MR, $\Delta\rho/\rho \equiv [\rho(B) - \rho(0)]/\rho(0)$, is positive (pMR) almost everywhere in samples with $x = 0$ and 0.13, as visible in Fig. 2(a,b), respectively. A small overall negative (nMR) effect with the maximum absolute values of ~4×10^{-5} at $T = 65$ K and ~3×10^{-6} at $T = 77$ K is observed at $x = 0$ only in fields below B ~3 − 4 T, decreasing rapidly with B and T. On the other hand, in samples with $x = 0.51$ and especially $x = 0.70$ the behavior of MR is quite different, as can be seen in Fig. 2(c,d), respectively. Namely, in the former pMR is observed in high fields at any temperature (Fig. 2(c)), whereas the nMR contribution appears with lowering B already at 180 K, which is visible in the inset to Fig. 2(c). The overall nMR effect is much stronger at $x = 0.51$ than at $x = 0$, attaining a maximum up to 6.6×10^{-4}. Moreover, below $B \sim 5$ T the dependence of nMR on T between 50–77 K is quite weak, shifting only the position of the nMR minimum to higher fields. In addition, the shape of the MR curves is different within various temperature intervals, exhibiting a substantial broadening above 77 K. The behavior of MR in the sample with $x = 0.70$ is even more complicated, exhibiting an increase of the nMR contribution with T increasing between 50–77 K, as evident in the inset to Fig. 2(d). Additionally, the overall nMR effect is higher at $x = 0.70$ than at $x = 0.51$, reaching the value of 1.5×10^{-3}. Generally, such features of nMR are quite uncommon for conventional

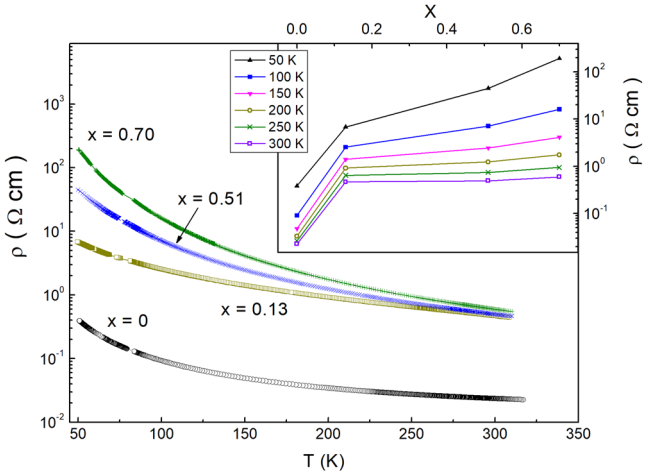

Figure 1. Temperature dependence of the resistivity in the investigated CZTGS samples. Inset: The plots of ρ vs. *x* at different temperatures. The lines simply connect the experimental data points.

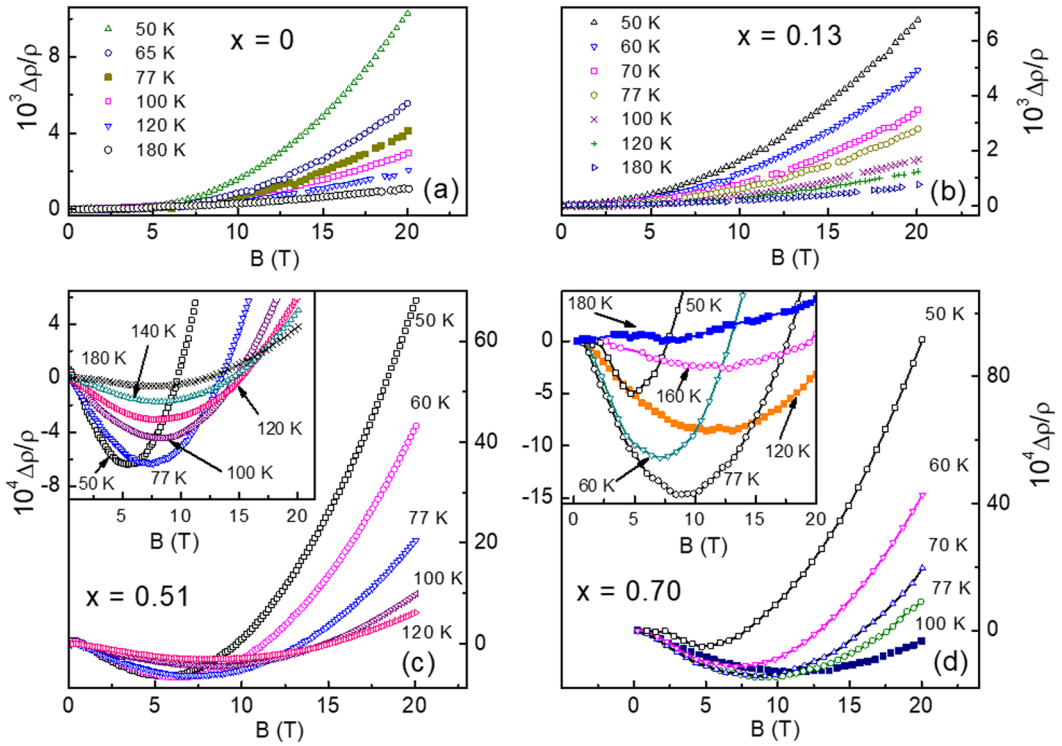

Figure 2. The dependences of Δρ/ρ on *B* for $x = 0$ (**a**), 0.13 (**b**), 0.51 (**c**) and $x = 0.70$ (**d**).

doped semiconductors. However, they have been already observed in the pure CZGS[24] and, partially, in the $Cu_2ZnSn_xGe_{1-x}Se_4$ alloys[32].

Temperature dependence of the resistivity at B = 0. In kesterites and related compounds, different mechanisms of the charge transfer have been observed within different temperature intervals ΔT[22–25,32–41]. These include (i) the nearest-neighbor hopping (NNH) at T lying within ΔT_n, (ii) the Mott VRH hopping inside the interval ΔT_M and (iii) thermal activation of charge carriers into an interval of delocalized states in the acceptor band at temperatures within ΔT_a[42–44]. In all cases above, ρ (T) is given by a universal expression,

$$\rho(T) = \rho_0(T)\exp\left[\left(\frac{T_0}{T}\right)^{1/p}\right], \quad (1)$$

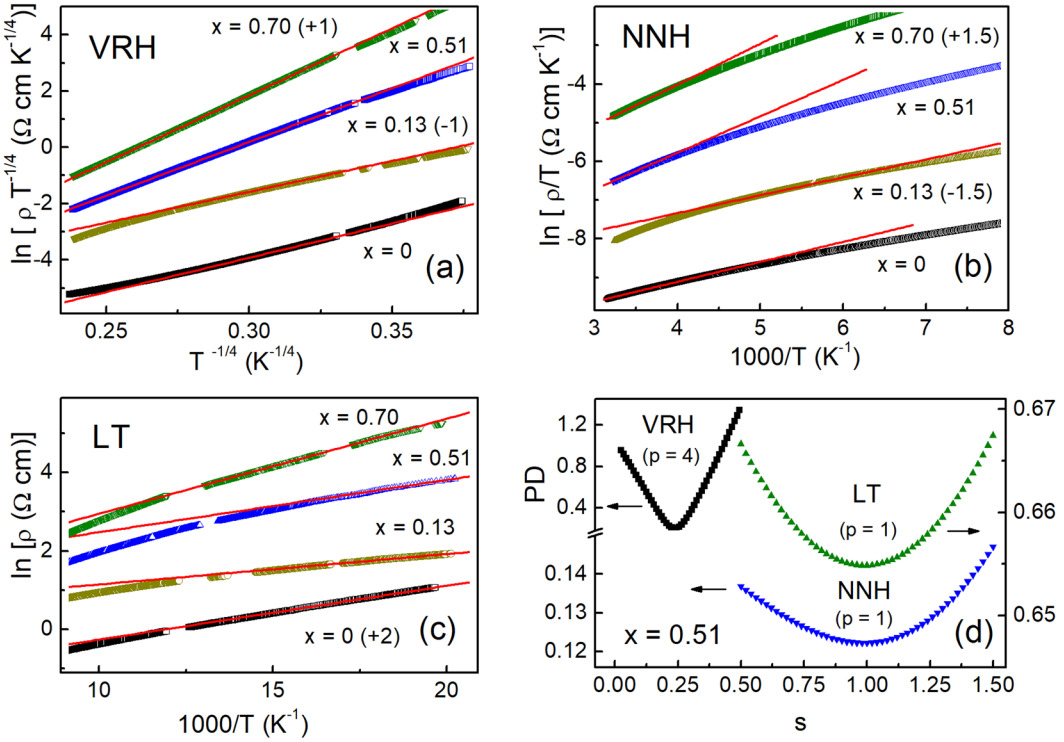

Figure 3. The plots of $\ln(\rho T^{-1/4})$ vs. $T^{-1/4}$ (**a**), the plots of $\ln(\rho/T)$ vs. $1000/T$ (**b**), the plots of $\ln(\rho)$ vs. $1000/T$ (**c**), and the plots of PD vs. s (**d**). Some of the plots are shifted along the vertical axes by the values, given in parenthesis, for convenience. The lines are linear fits.

x	ΔT_n (K)	ΔT_M (K)	ΔT_a (K)	m^*
0.00	265–310	95–145	50–65	0.49
0.13	170–195	80–150	50–60	0.60
0.51	270–310	95–180	50–60	0.54
0.70	265–310	80–165	55–75	0.51

Table 2. The temperature intervals ΔT_n, ΔT_M and ΔT_a of the NNH, VRH and LT conductivities, respectively, and the values of the effective mass, m^* (in units of m_0).

where $p = 1$ for the cases (i) and (iii), and $p = 4$ for the mechanism (ii). The prefactor $\rho_0(T) \propto T^{-1}$ for the NNH conduction, $\rho_0(T) \propto T^{-1/4}$ for the Mott VRH conduction, and $\rho_0 = \text{const}$ for the last out of the cases above. For the case (ii), the exponential factor of Eq. (1) is governed by the characteristic temperature, $T_0 = \beta/[k_B g(\mu) a^3]$, where $\beta = 21$, k_B is the Boltzmann constant, $g(\mu)$ is the density of states (DOS) at the Fermi level, μ, and a is the localization radius of charge carriers[42–44]. For the cases (i) and (iii), instead of T_0 the corresponding activation energies, $E_n = k_B T_0$ and $E_a = k_B T_0$ are used, respectively. Here, $E_a = |E_c - \mu|$, where E_c is the mobility edge of the acceptor band (AB) and μ is the Fermi energy[42,43].

In quaternary chalcogenides, the widest temperature interval belongs to the Mott VRH conduction[22–25]. Therefore, here we start the analysis of $\rho(T)$ by searching the interval ΔT_M and determination of T_0. As follows from Fig. 3(a), ρ(T) can be linearized according to Eq. (1) at $p = 4$ within intervals of ΔT_M (see Table 2). The values of T_0 have been obtained from the slopes of the plots in Fig. 3(a) and are shown in Fig. 4(a) as a function of x, along with the corresponding width of the AB, W, found with the expression $W \approx 0.5\, k_B\, (T_v^3\, T_0)^{1/4}$ [34,35]. Here, T_v is the onset of the VRH conduction on cooling (i. e. the right edge of the ΔT_M intervals in Table 2).

If μ lies close to the AB edge, the deviations of $\rho(T)$ from the Mott law above T_v can be explained by the transition to the NNH conduction (see above), where $E_n \approx W$[44]. As can be seen in Fig. 3(b), for all samples $\rho(T)$ can be linearized according to Eq. (1) at $p = 1$ within the intervals ΔT_n collected in Table 2. The values of E_n, obtained from the linear fit of the plots in Fig. 3(b) within the intervals ΔT_n, are displayed in Fig. 4(a) along with the W data, demonstrating a complete agreement with the latter at an error given by the size of the data points.

In turn, deviations of $\rho(T)$ in the low-temperature (LT) intervals, ΔT_a, lying below ΔT_M, are attributable to the case (iii) above. Indeed, the plots in Fig. 3(c) demonstrate a good linearity within intervals ΔT_a evidently below the temperatures of the Mott VRH conduction region (see Table 2) and yielding the data of E_a, displayed in Fig. 4(a).

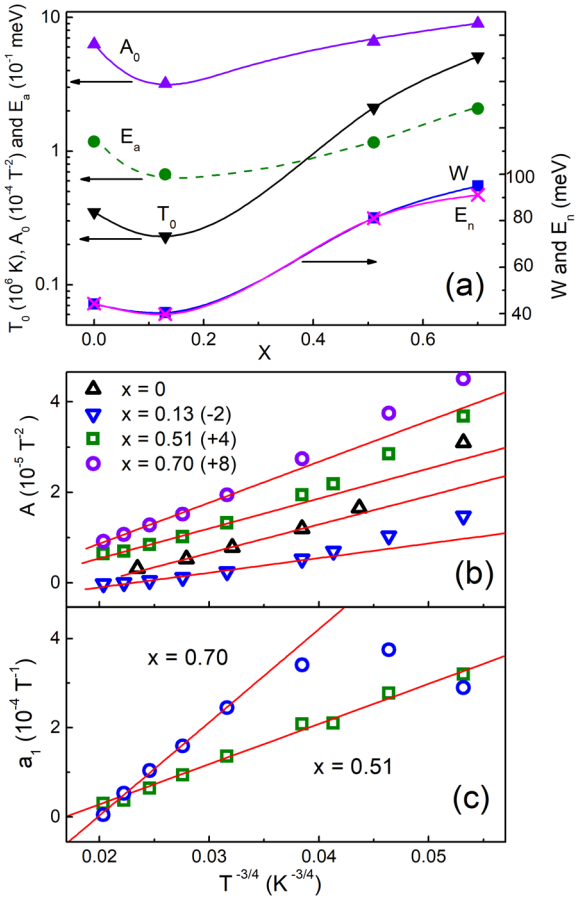

Figure 4. The plots of T_0, A_0, E_a, W and E_n vs. x. The lines are to guide the eye (**a**). The dependences of A on $T^{-3/4}$ for different x. Some of the data are shifted along the vertical axis by the values, given in parenthesis, for convenience. The lines are linear fits (**b**). The plots of a_1 vs. $T^{-3/4}$. The lines are linear fits (**c**).

Finally, the values of $s = 1/p$ were obtained with a "percentage deviation" (*PD*) method, where *PD* represents the relative difference between the experimental and calculated resistivity data[45]. This was done by minimizing *PD* inside the intervals ΔT_M, ΔT_n and ΔT_a, at different values of s (see refs[22,34] for details). We found a complete agreement between the values of s and $1/p$ for all samples. An example of such procedure is displayed in Fig. 3(d) for $x = 0.51$.

Analysis of the magnetoresistance. In the domain of the Mott VRH conduction, pMR is connected mainly to shrinkage of the impurity wave functions by the magnetic field[44]. In particular, this mechanism is the only one leading to pMR in weak magnetic fields of $\lambda \gg a$, where $\lambda = [\hbar/(eB)]^{1/2}$ is the magnetic length, $\hbar$ is the Planck constant and e is the elementary charge. Here, pMR is given by the expression

$$\ln\left[\frac{\rho(T, B)}{\rho(T, 0)}\right] = A(T)B^2, \tag{2}$$

where $A(T) = A_0\, T^{-3/4}$, $A_0 = t(e^2\, a^4/\hbar^2)T_0^{3/4}$ and $t = 5/2016$[44]. Because the overall nMR effect at $x = 0$ is small (see Section "Experimental results"), Eq. (2) can be utilized for the analysis of MR in this sample at least for the strong enough B values, where the nMR contribution is expected to be negligible. In the sample with $x = 0.13$ the overall nMR effect is not observed, so that Eq. (2) can be utilized without any restrictions, excluding only that of $\lambda \gg a$ mentioned above. However, at $x = 0.51$ and 0.70 the nMR contribution is increased to be taken into account more carefully.

As has been demonstrated recently[24,32], the most probable mechanism of nMR in CZGS is connected with quantum interference effects in the Mott VRH conduction interval[46–50]. Therefore, we can utilize this mechanism for interpretation of nMR in our CZTGS alloys, too, especially taking into account the close similarity of the MR behavior in both materials, mentioned in Section "Experimental results". Accordingly, for not too low magnetic fields nMR contribution can be written as $(\Delta\rho/\rho)_n = -a_1(T)B$, where $a_1(T) \propto T^{-3/4}$ similar to $A(T)$ above[49]. Taking into account the smallness of MR in our samples, providing a good accuracy for the approximative relation of $\ln[\rho(T,B)/\rho(T,0)] \approx \Delta\rho/\rho$, we can express pMR with Eq. (2) as $(\Delta\rho/\rho)_p = A(T)B^2$. Therefore, using the conventional expression of $\Delta\rho/\rho = (\Delta\rho/\rho)_n + (\Delta\rho/\rho)_p$, one finds the equation

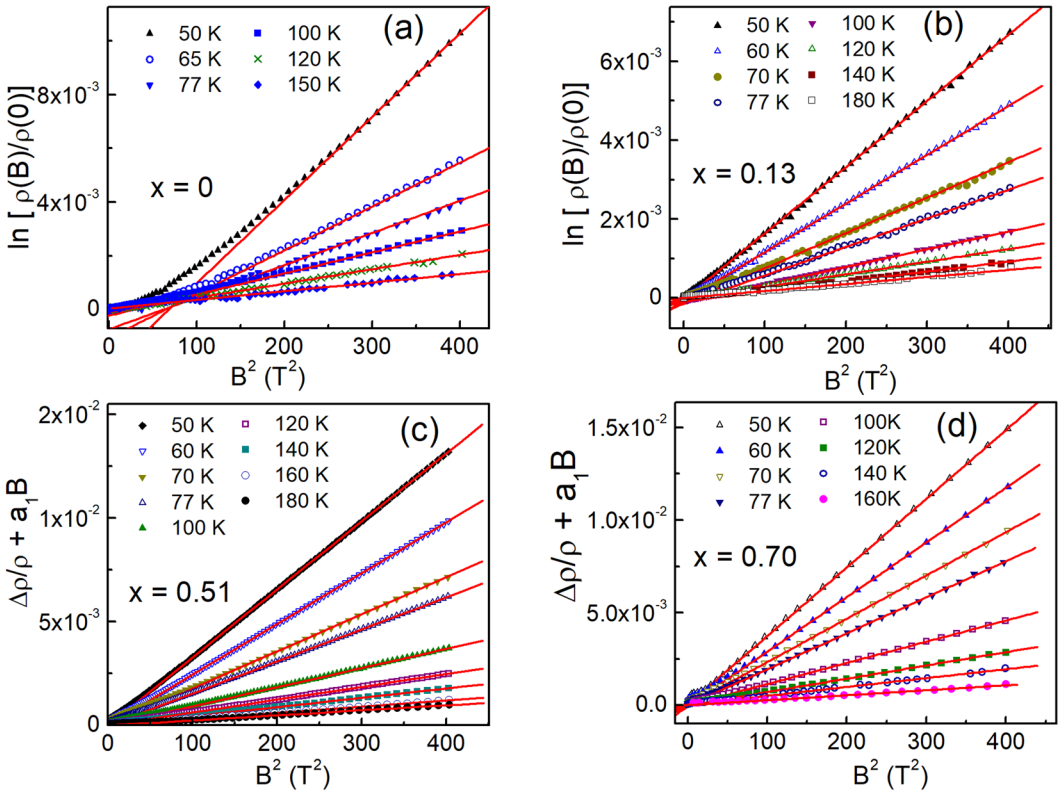

Figure 5. The plots of $\ln[\rho(B)/\rho(0)]$ vs. B^2 for $x = 0$ (**a**) and $x = 0.13$ (**b**). The plots of $\Delta\rho/\rho + a_1 B$ vs. B^2 for $x = 0.51$ (**c**) and $x = 0.70$ (**d**). The lines are linear fits.

$$\Delta\rho/\rho + a_1(T)B = A(T)B^2, \tag{3}$$

available for the analysis of MR in samples with $x = 0.51$ and 0.70, which can be performed here with the method, applied recently for CZGS[24]. Namely, the values of $a_1(T)$ can be found by plotting the left-hand side of Eq. (3) vs. B^2 and varying a_1 up to reach the best linearization of the plots. The latter can be done by minimizing the standard deviation (SD) of the plots, under an additional condition for the linear parts of the plots to pass through the origin[24].

Then, the values of $A(T)$ can be found from the slope of the plots shown in Fig. 5. Namely, this is provided by good linearity of these plots, excluding only the cases of $T = 50$ and 65 K in the sample with $x = 0$, deviating from the linearity with decreasing B, as seen in Fig. 5(a), due to a small nMR contribution (see Section "Experimental results"). However, this does not look to be a big problem, because the linear parts are still broad enough in the scale of Fig. 5(a) and, additionally, these temperature points lie outside the Mott VRH interval (cf. Table 2).

Eventually, the data of $A(T)$ are plotted vs. $T^{-3/4}$ in Fig. 4(b), exhibiting a good linearity within the whole interval ΔT_M of the Mott VRH conduction (cf. Table 2). A small deviation of the data point for $x = 0.5$ from the perfect linearity takes place only at $T = 180$ K (or $T^{-3/4} \approx 0.02\,K^{-3/4}$ in the scale of Fig. 4(b)) lying just on the border of ΔT_M. On the other hand, the stronger deviations of the plots in Fig. 4(b) from the linear behavior takes place in all samples with decreasing T, but this occurs already below ΔT_M (see Table 2). In addition, the dependences of $a_1(T) \propto T^{-3/4}$ also take place in both samples with $x = 0.51$ and 0.70, as can be seen in Fig. 4(c), violating only outside the Mott VRH conduction interval at $x = 0.70$.

Hence, in our material both the nMR and the pMR contributions to MR demonstrate the field and temperature dependences, which are in a complete agreement with mechanisms described above. Finally, the data of A_0 have been determined from the slope of the linear parts of the plots in Fig. 4(b) and are displayed in Fig. 4(a).

Determination of microscopic parameters and analysis of E_a. First of all, a pair of the parameters, a and $g(\mu)$, can be found directly with the pair of the corresponding expressions of T_0 and A_0, given in the text below Eqs (1) and (2), respectively. The obtained values of a and $g(\mu)$ are plotted vs. x in Fig. 6(a). Next, for the analysis of the E_a data and determination of further electronic parameters we use a general expression of a,

$$a = a_0(1 - N/N_C)^{-\nu}, \tag{4}$$

where N and N_C are the acceptor concentration and the critical concentration of the MIT, respectively[51]. Here, the value of the localization radius far from the MIT, a_0, is usually close to the Bohr radius, $a_B = \hbar^2\kappa_0/(m^* e^2)$[44], where

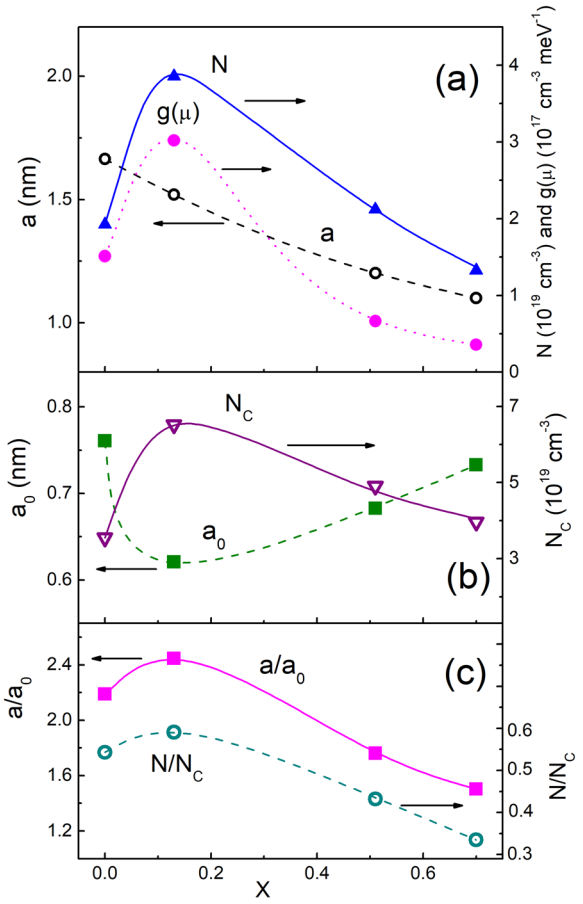

Figure 6. The dependences of a, $g(\mu)$ and N on x (**a**). The plots of a_0 and N_c vs. x (**b**). The dependences of a/a_0 and N/N_c on x (**c**). The lines are to guide the eye.

κ_0 is the dielectric permittivity of the material far from the MIT, m^* is the carrier effective mass and $\nu \approx 1$ is the critical exponent[51]. Another expression of the localization radius, is given by the equation[42,43].

$$a = a_0\left(1 - \frac{W + \mu}{W + E_c}\right)^{-\nu}. \tag{5}$$

Here, the energy is measured from the center of AB, E_A, which represents the mean energy of the acceptor levels, so that $\mu < E_c < 0$[24]. Finally, we approximate the DOS of AB with the Gaussian shape, which yields the expression.

$$g(\mu) = N/(\pi^{1/2}W)\exp[-(\mu/W)^2]. \tag{6}$$

The subsequent analysis of E_a can be performed with Eqs (4–6) by assuming the relation $a_0 = a_B$ at $\kappa_0 = 7$. Indeed, this value of κ_0 has been deduced from the capacitance spectra of CZTS[52], whereas the close data of $\kappa_0 = 6.68$ and 6.8 have been predicted with the first-principle calculations for CZGS with the KS and SN structures, respectively[53]. Therefore, the overall variation of κ_0 with x can be neglected, deviating from the value of $\kappa_0 = 7$ only by a few percent. Eventually, we use the universal Mott criterion, $N_C^{1/3}a_B \approx 0.25$[42,43].

Hence, the only unknown parameter, required for calculations of μ, E_c and, finally, E_a is the effective mass m^*. This parameter can be obtained by an explicit fit of the experimental E_a data with the expression $E_a = |\mu - E_c|$, using the following simple procedure: (i) taking a certain m^* value, one can evaluate $a_0 = a_B$ and N_C with the expression of a_B above and with the Mott criterion, respectively; (ii) then N can be obtained with Eq. (4) by utilization of the a data in Fig. 6(a); (iii) the knowledge of the parameters N and $g(\mu)$, where the data of $g(\mu)$ are displayed Fig. 6(a), too, permits determination of μ with Eq. (6); (iv) then, E_c can be calculate with Eq. (5); (v) finally, E_a can be found with the difference of μ and E_c, obtained above. Such procedure has been repeated for each of the E_a values in Fig. 4(a) by variation of m^* up to a complete agreement of the experimental and calculated E_a values, and the resulting data of m^* vs. x are presented in Fig. 7(a). For convenience, they are collected also in Table 2.

The obtained m^* values can be compared with the calculated data of the effective mass, using the mean values of $m = (m_t^2 m_l)^{1/3}$, which determine a_B in a case of the non-spherical carrier spectrum[44]. Here, m_t and m_l is the transversal and the longitudinal effective mass components, respectively, of the holes in the upmost valence band, which have been predicted for CZTS and CZGeS with the first-principle calculations[54]. Hence, using the data of

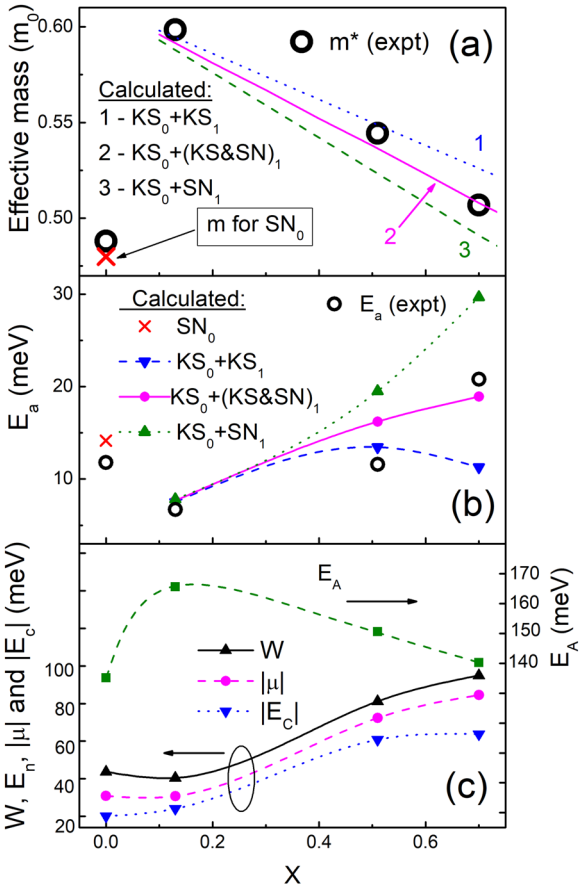

Figure 7. The plots of the experimental effective mass m^* vs. x (open circles). The lines 1–3 are evaluated as described in the text. The single oblique cross represents the effective mass value for the SN-CZGS phase (**a**). The dependence of the experimental activation energy E_a on x (open circles). The data given by the closed up triangles, closed circles and closed down triangles are evaluated, as described in the text. The lines are spline interpolations of the data points. The single oblique cross represents the E_a value, calculated with the effective mass of the SN-CZGS structure (**b**). The dependences of E_A, W, $|\mu|$ and $|E_c|$ on x. The lines are to guide the eye (**c**).

ref.[54] we find the following values (in units of the free electron mass, m_0): m_{KS} (CZGS) = 0.61, m_{SN} (CZGS) = 0.48, m_{KS} (CZTS) = 0.49 and m_{SN} (CZTS) = 0.44, for the KS-CZGS, SN-CZGS, KS-CZTS and SN-CZTS phases, respectively.

The comparison of the data above with the values of m^* in Table 2 indicates a close proximity of m^* at $x = 0$ to m_{SN}(CZGS), whereas m^* at $x = 0.13$ is much closer to m_{KS}(CZGS). In turn, for x between 0.13 and 0.70 the data of m^* are lying between those of m_{KS}(CZGS) and m_{KS}(CZTS) or m_{SN}(CZTS). Then, to account for a gradual variation of the phase content in CZTGS with x, we apply the linear dependences of the mean effective mass between $x = 0.13$ and 0.70 in the following forms: $m(KS_0 + KS_1) = m_{KS}(CZGS) + [m_{KS}(CZTS) - m_{KS}(CZGS)]x$, $m[KS_0 + (KS\&SN)_1] = m_{KS}(CZGS) + \{[m_{KS}(CZTS) + m_{SN}(CZTS)]/2 - m_{KS}(CZGS)\}x$, and $m(KS_0 + SN_1) = m_{KS}(CZGS) + [m_{SN}(CZTS) - m_{KS}(CZGS)]x$. Such dependences covering different possible phases of the border compounds at $x = 0$ and 1 (given above by the subscripts 0 and 1, respectively), including a mixed KS and SN phase denoted here as KS&SN, are plotted in Fig. 7(a) with the straight lines along with the experimental m^* data (open circles). The data point for the pure SN-CZGS mass (single oblique cross) is added to Fig. 7(a) for completeness.

As follows from Fig. 7(a), the contribution of the SN-CZTS phase is out of game, because $m(KS_0 + SN_1)$ (line 3) is close to m^* only at $x = 0.13$, where the impacts of any CZTS phases are simply too small. This means that the SN-CZTS phase, being less stable in the pure CZTS compound than the KS-CZTS phase[28–30], cannot be stabilized even by introduction of Ge. On the other hand, a coincidence of $m[KS_0 + (KS\&SN)_1]$ (line 2) with m^* at $x = 0.70$ suggests a more importance of the mixed KS and SN structure of CZTS, contributing to the CZTGS alloy phase content, than that of the pure KS-CZTS phase (line 1 lies clearly above m^* at $x = 0.70$). Eventually, both lines 1 and 2 lie equivalently around the data point of m^* at $x = 0.51$, which does not permit to make a comprehensive conclusion at this point of the CZTGS alloy, because the mixed (KS&SN)-CZTS phase, generally, cannot coexist with the pure KS-CZTS phase.

On the other hand, the issue above can be clarified by the direct calculation of E_a vs. x with the linear dependences of the effective mass between $x = 0.13$ and 0.70 given above, being performed without any fitting procedure, as displayed in Fig. 7(b). Here, the calculations can be realized only at selected values of x, and the lines

in Fig. 7(b) are only the spline interpolations of the data evaluated at $x = 0.13$, 0.51 and 0.70, respectively. The calculated value of E_a at $x = 0$ with m_{SN}(CZGS) is also presented in Fig. 7(b) with the oblique cross point, exhibiting a reasonable agreement with the experimental E_a value. The contribution of the SN-CZTS phase (closed up triangles) to E_a does not exist again, since at $x = 0.51$ and 0.70 the corresponding calculated values lie substantially above both these experimental data points. The calculated E_a value for the mixed (KS&SN)-CZTS phase (closed circles) lie close to the experimental data point at $x = 0.70$, which confirms the main role of this phase in formation of the alloy structure at this composition, following from Fig. 7(a). On the other hand, the calculated E_a value for the pure KS-CZTS phase (closed down triangles) satisfies the experimental E_a value at $x = 0.51$ much better, than for the mixed (KS&SN)-CZTS phase. This reflects the dominating contribution of the pure KS-CZTS phase at $x = 0.51$, which removes the ambiguity at this point in Fig. 7(a).

Finally, the parameters following from the explicit fit of E_a above, including N, N_c and a_0, as well as the ratios of N/N_c and a/a_0, are displayed in Fig. 6(a–c), respectively. In addition, the data of E_c and μ are given in Fig. 7(c) along with the W values. The data of E_A, evaluated with the expression for hydrogenic acceptor level, $E_A = \hbar^2/(2m^* a_0^2)$[44], are presented in Fig. 7(a), too.

Discussion

First, the conductivity mechanisms have been determined within temperature intervals ΔT_n, ΔT_v and ΔT_a with two different methods, including linearization of the $\rho(T)$ data in Fig. 3 (a–c) and application of the percentage deviation method in Fig. 3 (d). The results obtained with both methods are mutually consistent. This provides evidence for the NNH and VRH charge transfer within the temperature intervals ΔT_n and ΔT_v, respectively. A special attention has been paid to the LT conduction mechanism, characterized by the activation energy E_a.

Namely, we have found that the values of E_a obtained in the LT region of ΔT_a above, exhibit a reasonable agreement with those calculated with the expression of $E_a = |\mu - E_c|$ in previous Section. This gives a strong support to the nature of the low-temperature activated conductivity mechanism, acting below the Mott VRH conduction temperatures within ΔT_M (Table 2), and connected with thermal activation of holes into the region of the delocalized states of AB (see previous Section). It is important to note, that E_a appears to be rather sensitive to the details of the CZTGS alloy structure, which is evident from previous Section and permits estimation of contributions of the different CZGS and CZTS phases to the CZTGS alloy structure. In particular, a steep increase of $\rho(x)$ between $x = 0$ and 0.13, ascribed tentatively in Section "Experimental results" to the possible transition from the SN to KS phase of CZGS and followed by a weaker $\rho(x)$ dependence between $x = 0.13$–0.70, finds a convincing explanation by the analysis of $E_a(x)$.

Next, the joint analysis of the $\rho(T)$ and pMR data permitted determination of such important microscopic parameters as W, E_C and $g(\mu)$, characterizing the energy spectrum of the holes in AB, as well as those of a, N, N_C and E_A. As can be seen in Figs 4, 6 and 7, the majority of these parameters (excluding only E_C) exhibit extremums near $x = 0.13$, similar to those of $\rho(x)$ and $E_a(x)$ in Figs 1 and 7(b), respectively. This suggests a similar reason for such extremums, reflecting the transition above, too. On the other hand, the cation ratios in the analyzed samples are also not constant and reaches the maximum for the sample with $x = 0.13$ (see the values in the last three columns of Table 1). Taking into account the overwhelming effect of Cu_{Zn} defects to the AB formation[55–58], the influence of Cu/Zn ratio should be always considered in the quaternary compounds containing these cations.

As can be seen in Fig. 6(c), samples with different x are characterized by various values of N/N_C and a/a_0, implying their different proximity to the MIT according to Eq. (4). This supports completely the corresponding conjecture formulated in the beginning of Section "Experimental results".

Finally, as follows from Fig. 2 and the corresponding discussion in Section "Experimental results", nMR at $x = 0$ is quite small, whereas at $x = 0.13$ it is even absent. At the same time, nMR for $x = 0.51$ becomes important, and at $x = 0.70$, closest to CZTS, nMR attains the maximum value. The reason to such behavior is that nMR due to the quantum interference effects in the VRH conduction domain is highly sensitive to the degree of disorder[46], which is indicated by the W value. As can be seen in Fig. 4(a), W in samples with $x = 0$ and 0.13 is substantially smaller, than in those with $x = 0.51$ and 0.70, which is in line with the strong sensitivity of nMR to the disorder, mentioned above.

Conclusions

We have investigated the resistivity and the magnetoresistance in the $Cu_2ZnSn_xGe_{1-x}S_4$ single crystals. The analysis of the $\rho(T)$ and MR data permits identification of the conductivity mechanisms within different temperature intervals between $T \sim 50$–300 K. Namely, at high temperatures the conduction is realized by the NNH charge transfer, followed by the Mott VRH conduction with decreasing temperature, and eventually by the activation of holes into the interval of delocalized states of the acceptor band, observed within the lowest temperature interval. Detailed analysis of the activation energy in the latter interval gives evidence for the transition of CZTGS from the SN phase to a KS phase with increasing x between 0–0.13, and the subsequent smooth evolution of the material within a KS-like structure. The contributions of different phases, pertinent to the border compounds, to the mixed-phase alloy state have been estimated. The values of the important microscopic parameters of the material, including width of the acceptor band, the localization radius and the density of states at the Fermi level, as well as the acceptor concentration have been determined. All the parameters above exhibit extremums near $x = 0.13$, which is connected mainly to the crystalline structure phase transformation near this point, as well as to the possible influence of the Cu/Zn ratio.

References

1. Qi, Y.-F. *et al*. Engineering of interface band bending and defects elimination via Ag-graded active layer for efficient $(Cu,Ag)_2ZnSn(S,Se)_4$ solar cells. *Energy Environ. Sci.* **10**, 2401–2410 (2017).
2. Shin, D. *et al*. Earth-abundant chalcogenide photovoltaic devices with over 5% efficiency based on a $Cu_2BaSn(S,Se)_4$ absorber. *Adv. Mater.* **29**, 1606945 (2017).

3. Yan, C. *et al*. Beyond 11% efficient sulfide kesterite $Cu_2Zn_xCd_{1-x}SnS_4$ solar cell: effects of cadmium alloying. *ACS Energy Lett.* **2**, 930–936 (2017).
4. Giraldo, S. *et al*. How small amounts of Ge modify the formation pathways and crystallization of kesterites. *Energy Environ. Sci.* **11**, 582–593 (2018).
5. Guo, Q. *et al*. Enhancing the performance of CZTSSe solar cells with Ge alloying. *Sol. Energy Mater. Sol. Cells* **105**, 132–136 (2012).
6. Kim, I. *et al*. Bandgap-graded $Cu_2Zn(Sn_{1-x}Ge_x)S_4$ thin-film solar cells derived from metal chalcogenide complex ligand capped nanocrystals. *Chem. Mater.* **26**, 3957–3965 (2014).
7. Hages, C. J. *et al*. Improved performance of Ge-alloyed CZTGeSSe thin film solar cells through control of elemental losses. *Prog. Photovolt: Res. Appl.* **23**, 376–384 (2015).
8. Giraldo, S. *et al*. Large efficiency improvement in $Cu_2ZnSnSe_4$ solar cells by introducing a superficial Ge nanolayer. *Adv. Energy Mater.* **5**, 1501070 (2015).
9. León, M. *et al*. Optical constants of Cu_2ZnGeS_4 bulk crystals. *J. Appl. Phys.* **108**, 093502 (2010).
10. Levcenco, S., Dumcenco, D., Huang, Y. S., Tiong, K. K. & Du, C. H. Anisotropy of the spectroscopy properties of the wurtz-stannite Cu_2ZnGeS_4 single crystals. *Opt. Mater.* **34**, 183–188 (2011).
11. Caballero, R. *et al*. Band-gap engineering of $Cu_2ZnSn_{1-x}GexS_4$ single crystals and influence of the surface properties. *Acta Materialia* **79**, 181–187 (2014).
12. Khadka, D. B. & Kim, J. H. Band gap engineering of alloyed $Cu_2ZnGe_xSn_{1-x}Q_4$ (Q = S,Se) films for solar cell. *J. Phys. Chem. C* **119**, 1706–1713 (2015).
13. Garcia-Llamas, E. *et al*. Wide band-gap tuning $Cu_2ZnSn_{1-x}Ge_xS_4$ single crystals: Optical and vibrational properties. *Sol. Energy Mater. Sol. Cells* **158**, 147–153 (2016).
14. Umehara, M., Tajima, S., Takeda, Y. & Motohiro, T. Wide bandgap $Cu_2ZnSn_{1-x}Ge_xS_4$ fabricated on transparent conductive oxide-coated substrates for top-cells of multi-junction solar cells. *J. Alloy Compd.* **689**, 713–717 (2016).
15. Chen, J. *et al*. $Cu_2ZnSn_xGe_{1-x}S4$ thin film Solar Cell by Sulfurizing Sputtered Metallic Precursors. *Proceedings of 29th European Photovoltaic Solar Energy Conference and Exhibition*, Amsterdam, Netherlands, 1752–1755 (2014).
16. Chen, J., Li, W., Yan, C., Huang, S. & Hao, X. Studies of compositional dependent $Cu_2Zn(Ge_xSn_{1-x})S_4$ thin films prepared by sulfurizing sputtered metallic precursors. *J. Alloy Compd.* **621**, 154–161 (2015).
17. Caballero, R. *et al*. Towards the growth of $Cu_2ZnSn_{1-x}Ge_xS_4$ thin films by a single-stage process: Effect of substrate temperature and composition. *Sol. Energy Mater. Sol. Cells* **139**, 1–9 (2015).
18. Garcia-Llamas, E. *et al*. Multiwavelength excitation Raman scattering of $Cu_2ZnSn_{1-x}Ge_x(S,Se)_4$ single crystals for earth abundant photovoltaic applications. *J. Alloy Compd.* **692**, 249–256 (2017).
19. Valakh, M. Y. *et al*. Optical properties of quaternary kesterite-type $Cu_2Zn(Sn_{1-x}Ge_x)S_4$ crystalline alloys: Raman scattering, photoluminescence and first-principle calculations. *RSC Adv.* **6**, 67756–67763 (2016).
20. Kosyak, V., Karmarkar, M. A. & Scarpulla, M. A. Temperature dependent conductivity of polycrystalline Cu_2ZnSnS_4 thin films. *Appl. Phys. Lett.* **100**, 263903 (2012).
21. Nagaoka, A., Miyake, H., Taniyama, T., Kakimoto, K. & Yoshino, K. Correlation between intrinsic defects and electrical properties in the high-quality Cu_2ZnSnS_4 single crystal. *Appl. Phys. Lett.* **103**, 112107 (2013).
22. Lähderanta, E., Guc, M., Shakhov, M. A., Arushanov, E. & Lisunov, K. G. Influence of scattering and interference effects on the low-temperature magnetotransport of Cu_2ZnSnS_4 single crystals. *J. Appl. Phys.* **120**, 035704 (2016).
23. Lähderanta, E. *et al*. High-field hopping magnetotransport in kesterites. *J. Magn. Magn. Mater*. **459**, 246–251 (2018).
24. Guc, M. *et al*. Mechanisms of charge transfer and electronic properties of Cu_2ZnGeS_4 from investigations of the high-field magnetotransport. *Sci. Rep.* **7**, 10685 (2017).
25. Hajdeu-Chicarosh, E. Variable-range hopping conduction in the kesterite and wurtzstannite Cu_2ZnGeS_4 single crystals. *Surf. Engin. Appl. Electrochem.* **54**, 279–285 (2018).
26. Guc, M. *et al*. Optical phonons in the kesterite Cu_2ZnGeS_4 semiconductor: polarized Raman spectroscopy and first-principle calculations. *RSC Adv.* **6**, 13278–13285 (2016).
27. Guc, M. *et al*. Optical phonons in wurtzstannite Cu_2ZnGeS_4 semiconductor: polarized Raman spectroscopy and first principle calculations. *Phys. Rev. B* **89**, 205205 (2014).
28. Schorr, S., Hoebler, H.-J. & Tovar, M. A neutron diffraction study of the stannite-kesterite solid solution series. *Eur. J. Mineral.* **19**, 65–73 (2007).
29. Persson, C. Electronic and optical properties of Cu_2ZnSnS_4 and $Cu_2ZnSnSe_4$. *J. Appl. Phys.* **107**, 053710 (2010).
30. Lafond, A. *et al*. X-ray resonant single-crystal diffraction technique, a powerful tool to investigate the kesterite structure of the photovoltaic Cu_2ZnSnS_4 compound. *Acta Crystallogr., Sect. B* **70**, 390–394 (2014).
31. Nagoya, A., Asahi, R., Wahl, R. & Kresse, G. Defect formation and phase stability of Cu_2ZnSnS_4 photovoltaic material. *Phys. Rev. B* **81**, 113202 (2010).
32. Lähderanta, E. *et al*. Hopping magnetotransport of the band-gap tuning $Cu_2Zn(Sn_xGe_{1-x})Se_4$ crystals. *J. Phys.: Condens. Mat.* **28**, 455801 (2016).
33. Hajdeu-Chicarosh, E. *et al*. Mechanisms of conductivity and energy spectrum of near-edge holes in Cu_2ZnSnS_4 powder samples. *J. Alloy Compd.* **703**, 315–320 (2017).
34. Lisunov, K. G. *et al*. Features of the acceptor band and properties of localized carriers from studies of the variable-range hopping conduction in single crystals of p-Cu_2ZnSnS_4. *Sol. Energy Mater. Sol. Cell* **112**, 127–133 (2013).
35. Lisunov, K. G. *et al*. Energy spectrum of near-edge holes and conduction mechanisms in $Cu_2ZnSiSe_4$ single crystals. *J. Alloys Compd.* **580**, 481–486 (2013).
36. Guc, M. *et al*. Transport properties of kesterite thin films of Cu_2ZnSnS_4 obtained by spray pyrolysis. *Proceedings of 28th European Photovoltaic Solar Energy Conference and Exhibition*, Paris, France, 2449–2452 (2013).
37. Guc, M. *et al*. Disorder and variable-range hopping conductivity in Cu_2ZnSnS_4 thin films prepared by flash evaporation and post-thermal treatment. *J. Alloy Compd.* **596**, 140–144 (2014).
38. Dermenji, L. *et al*. Influence of the annealing process on transport and photoelectrical properties of Cu_2ZnSnS_4 kesterite thin films obtained by spray pyrolysis. *Proceedings of 29th European Photovoltaic Solar Energy Conference and Exhibition*, Amsterdam, Netherlands, 1801–1804 (2014).
39. González, J. C. *et al*. Influence of the sulphurization time on the morphological, chemical, structural and electrical properties of Cu_2ZnSnS_4 polycrystalline thin films. *Sol. Energy Mater. Sol. Cell* **123**, 58–64 (2014).
40. Ansari, M. Z. & Khare, N. Thermally activated band conduction and variable range hopping conduction in Cu_2ZnSnS_4 thin films. *J. Appl. Phys.* **117**, 025706 (2015).
41. Hazama, H., Tajima, S., Masuoka, Y. & Asahi, R. Transport properties of the Cu_2ZnSnS_4 bulk systems: Effects of nonstoichiometry and defect formation. *J. Alloys Compd.* **657**, 179–183 (2016).
42. Mott, N. F. & Davies, E. A. *Electron Processes in Non-Crystalline Materials* (Clarendon, Oxford, 1979).
43. Mott, N. F. *Metal–Insulator Transitions* (Taylor and Francis, London, 1990).
44. Shklovskii, B. I. & Efros, A. L. *Electronic Properties of Doped Semiconductors* (Springer, Berlin, 1984).
45. Finlayson, D. M. & Mason, P. J. Variable-range hopping in indium phosphide. *J. Phys. C: Solid State Physics* **19**, L299–L301 (1086).
46. Shklovskii, B. I. & Spivak, B. Z. Scattering and interference effects in variable range hopping conduction. In *Hopping Transport in Solids* (eds Pollak, M. & Shklovskii, B.) 271–349 (North-Holland, Amsterdam, 1991).

47. Nguen, V. L., Spivak, B. Z. & Shklovskii, B. I. Tunnel hopping in disordered systems. *Sov. Phys. JETP* **62**, 1021–1029 (1985).
48. Sivan, U., Entin-Wohlman, O. & Imry, Y. Orbital magnetoconductance in the variable-range–hopping regime. *Phys. Rev. Lett.* **60**, 1566 (1988).
49. Raikh, M. E. & Wessels, G. F. Single-scattering-path approach to the negative magnetoresistance in the variable-range-hopping regime for two-dimensional electron systems. *Phys. Rev. B* **47**, 15609 (1993).
50. Medina, E. & Kardar, M. Quantum interference effects for strongly localized electrons. *Phys. Rev. B* **46**, 9984 (1992).
51. Castner, T. G. Hopping conduction in the critical regime approaching the metal-insulator transition. In *Hopping Transport in Solids* (eds Pollak, M. & Shklovskii, B.) 1–49 (North-Holland, Amsterdam, 1991).
52. Gunavan, O. *et al*. Electronic properties of the $Cu_2ZnSn(Se,S)_4$ absorber layer in solar cells as revealed by admittance spectroscopy and related methods. *Appl. Phys. Lett.* **100**, 253905 (2012).
53. Chen, D. & Ravindra, N. M. Electronic and optical properties of Cu_2ZnGeX_4 (X = S, Se and Te) quaternary semiconductors. *J. Alloys Compd.* **579**, 468–472 (2013).
54. Liu, H.-R. *et al*. First-principles study on the effective masses of zinc-blend-derived Cu_2Zn-IV-VI_4 (IV = Sn, Ge, Si and VI = S, Se). *J. Appl. Phys.* **112**, 093717 (2012).
55. Levcenko, S. *et al*. Photoluminescence characterization of Cu_2ZnGeS_4 single crystals. *Phys. Stat. Sol. C* **10**, 1079–1081 (2013).
56. Levcenko, S., Tezlevan, V. E., Arushanov, E., Schorr, S. & Unold, T. Free-to-bound recombination in near stoichiometric Cu_2ZnSnS_4 single crystals. *Phys. Rev. B* **86**, 045206 (2012).
57. Chen, S., Walsh, A., Gong, X.-G. & Wei, S.-H. Classification of lattice defects in the kesterite Cu_2ZnSnS_4 and $Cu_2ZnSnSe_4$ earth-abundant solar cell absorbers. *Adv. Mater.* **25**, 1522–1539 (2013).
58. Chen, S., Yang, J.-H., Gong, X. G., Walsh, A. & Wei, S.-H. Intrinsic point defects and complexes in the quaternary kesterite semiconductor Cu_2ZnSnS_4. *Phys. Rev. B* **81**, 245204 (2010).

Acknowledgements

The research leading to the presented results has been partially supported by the INFINITE-CELL project. This project has received funding from the European Union's Horizon 2020 research and innovation programme under the Marie Skłodowska-Curie Grant Agreement No. H2020-MSCA-RISE-2017-777968. Authors from the Institute of Applied Physics appreciate the financial supports from STCU 6224 and from the Institutional Project CSSDT 15.817.02.04A. Elena Hajdeu-Chicarosh acknowledges the World Federation of Scientists National Scholarship Program.

Author Contributions

I.V.B. grown the single crystals. E.H.-C. and I.Z. performed the resistivity and magnetoresistance measurements. M.A.S. supervised the experimental process and discussed the results. M.G. and E.H.-C. carried out the preliminary data analysis. K.G.L. performed the major part of analysis of experimental data and wrote the article. E.A. and E.L. supervised the whole work, discussed the results and commented on the manuscript. All authors reviewed the manuscript.

Additional Information

Competing Interests: The authors declare no competing interests.

Publisher's note: Springer Nature remains neutral with regard to jurisdictional claims in published maps and institutional affiliations.